This is a preprint, the final version is subject to change, of the American Mineralogist (MSA)
Cite as Authors (Year) Title. American Mineralogist, in press.
DOI: https://doi.org/10.2138/am-2018-6527

Revision 2

Anisotropic Thermoelastic Properties of Fe_7C_3 at High Pressures by Single-Crystal X-Ray Diffraction

XIAOJING LAI[1, 2, *], FENG ZHU[3], JIACHAO LIU[4], DONGZHOU ZHANG[2], YI HU[1, 2], GREGORY J. FINKELSTEIN[2], PRZEMYSLAW DERA[2], BIN CHEN[2,*]

[1]Department of Geology and Geophysics, University of Hawai'i at Mānoa, Honolulu, Hawaii, 96822, USA

[2]Hawaii Institute of Geophysics and Planetology, University of Hawai'i at Mānoa, Honolulu, Hawaii, 96822, USA

[3]Department of Earth and Environmental Science, University of Michigan, Ann Arbor, 48109, Michigan, USA

[4]Department of Geological Sciences, Jackson School of Geosciences, University of Texas at Austin, Austin, Texas, 78712, USA

*Corresponding Authors:

Xiaojing Lai (laixiaoj@hawaii.edu)

Bin Chen (binchen@hawaii.edu)

This is a preprint, the final version is subject to change, of the American Mineralogist (MSA)
Cite as Authors (Year) Title. American Mineralogist, in press.
DOI: https://doi.org/10.2138/am-2018-6527

Revision 2

ABSTRACT

Carbon has been suggested as one of the light elements existing in Earth's core. Under core conditions, iron carbide Fe_7C_3 is likely the first phase to solidify from an Fe-C melt and has thus been considered a potential component of the inner core. The crystal structure of Fe_7C_3, however, is still under debate, and its thermoelastic properties are not well constrained at high pressures. In this study, we performed synchrotron-based single-crystal X-ray diffraction experiment using an externally-heated diamond anvil cell to determine the crystal structure and thermoelastic properties of Fe_7C_3 up to 80 GPa and 800K. Our diffraction data indicate that Fe_7C_3 adopts an orthorhombic structure under experimentally investigated conditions. The pressure-volume-temperature data for Fe_7C_3 were fitted by the high-temperature Birch-Murnaghan equation of state, yielding ambient-pressure unit cell volume V_0 = 745.2(2) Å^3, bulk modulus K_0 = 167(4) GPa, its first pressure derivative K_0' = 5.0(2), dK/dT = -0.02(1) GPa/K, and thermal expansion relation $\alpha_T = 4.7(9)\times10^{-5}+3(5\times)10^{-8}\times(T\text{-}300)$ K^{-1}. We also observed an anisotropic elastic response to changes in pressure and temperature along the different crystallographic directions. Fe_7C_3 has strong anisotropic compressibilities with the linear moduli $M_a > M_c > M_b$ from zero pressure to core pressures at 300K, rendering the b axis the most compressible upon compression. The thermal expansion of c^3 is approximately four times larger than that of a^3 and b^3 at 600K and 700K, implying that the high temperature may significantly influence the elastic anisotropy of Fe_7C_3. Therefore the effect of high temperature needs to be considered when using Fe_7C_3 to explain the anisotropy of Earth's inner core.

This is a preprint, the final version is subject to change, of the American Mineralogist (MSA)
Cite as Authors (Year) Title. American Mineralogist, in press.
DOI: https://doi.org/10.2138/am-2018-6527

Revision 2

Key words : iron carbide, thermal equation of state, anisotropy, inner core, temperature effect

INTRODCUTION

Earth's inner core is considered to consist primarily of iron alloyed with nickel and one or more light elements e.g. sulfur, silicon, oxygen, hydrogen and carbon, as informed by numerous geophysical and geochemical constraints (recently reviewed by Hirose et al., 2013; Li and Fei, 2014; Litasov and Shatskiy, 2016). The Fe-C system has been proposed as a candidate composition for Earth's core largely due to the high cosmochemical abundance of carbon, the frequent occurrence of iron carbide phases in meteorites, and the high solubility of carbon in Fe-Ni liquids under the core-mantle differentiation conditions (Wood, 1993). If the liquid core contained carbon, the iron carbide phase, Fe_7C_3, may be the first phase to crystallize from the iron-carbon melt under core conditions rather than other iron carbide phases such as Fe_3C, as suggested by previously published Fe-C phase diagrams (Fei and Brosh, 2014; Lord et al., 2009; Nakajima et al., 2009). The extrapolated density and sound velocity of Fe_7C_3 may account for the density deficit and low S-wave velocity (v_s) of the inner core (Chen et al., 2012; Chen et al., 2014; Liu et al., 2016a; Nakajima et al., 2011). In addition, its high Poisson's ratio at inner core conditions was suggested to be comparable to that of the inner core (Prescher et al., 2015). Moreover, the melting experiments by Liu et al. (2016b) suggested that Fe_7C_3 may be a constituent of the innermost inner core for carbon-bearing core composition due to its high melting temperature.

This is a preprint, the final version is subject to change, of the American Mineralogist (MSA)
Cite as Authors (Year) Title. American Mineralogist, in press.
DOI: https://doi.org/10.2138/am-2018-6527

The crystal structure of Fe_7C_3 has remained controversial over the last few decades. Previous experimental studies reported its structure as either hexagonal ($P6_3mc$) (Herbstein and Snyman, 1964) or orthorhombic (*Pnma*, $Pmn2_1$, $Pmc2_1$, *Pmcn* or *Pbca*) (Barinov et al., 2010; Bouchard, 1967; Fruchart et al., 1965; Prescher et al., 2015). Theoretical calculations also compared the stability of hexagonal and orthorhombic phases. Fang et al. (2009) determined that the orthorhombic phase (*Pnma*) is more stable than the hexagonal phase ($P6_3mc$), whereas Raza et al. (2015) calculated that the orthorhombic phase (space group *Pbca*) is the stable phase below 100 GPa and the hexagonal phase becomes more stable above 100 GPa.

The elastic constants of Fe_7C_3 were also calculated at 0K for the two crystal structures with space groups of $P6_3mc$ and *Pbca* (Mookherjee et al., 2011; Raza et al., 2015). There has been, however, only one study that calculated the thermoelasticity of Fe_7C_3 with the space group of $P6_3mc$ (Li et al., 2016). Most of the high-pressure experimental studies of the density of Fe_7C_3 were performed at room temperature. The thermal equation of state (EoS) parameters have only been determined below 30 GPa (Litasov et al., 2015; Nakajima et al., 2011), which leads to a large uncertainty when extrapolating the experimental data to the pressure and temperature (*P*-*T*) conditions of the inner core. Accurate knowledge on the crystal structure and themoelastic properties of Fe_7C_3 under core conditions is needed to construct a comprehensive and seismologically consistent Fe-C inner core compositional model.

For the inner core, seismic waves travel faster along the rotational axis than in the equatorial plane; one possible explanation for this anisotropy is the presence of preferentially-orientated iron with strong single-crystal elastic anisotropy in Earth's inner

This is a preprint, the final version is subject to change, of the American Mineralogist (MSA)
Cite as Authors (Year) Title. American Mineralogist, in press.
DOI: https://doi.org/10.2138/am-2018-6527

core (Deuss, 2014; Hirose et al., 2013). The alloying of light elements with iron often leads to different crystal structure and elasticity (Litasov and Shatskiy, 2016). Thus, quantification of the elastic anisotropy of iron alloys is essential for us to understand the inner-core anisotropy. For *hcp* metals and isostructural iron alloys such as Fe-Ni-Si system, the elastic anisotropy is related to the *c*/*a* ratio, that is, the compressibilities and thermal expansion of the *a* and *c* unit cell parameters under high pressure and high temperature (Fischer and Campbell, 2015; Steinle-Neumann et al., 2001; Wenk et al., 1988). For orthorhombic Fe_7C_3, the elastic anisotropy is also correlated with the different compressional response to applied pressure of each primary crystallographic axis as reported in a calculation by Raza et al. (2015). Therefore, it is crucial to constrain how the compressibility and thermal expansion along individual crystallographic axes respond to pressure and temperature, so as to understand the potential for this material to contribute to the seismic anisotropy observed in the inner core (Deuss, 2014). In this study, we determined the thermal EoS and the thermoelastic properties of Fe_7C_3 along different crystallographic axes up to 80 GPa and 800K by employing an externally-heated diamond anvil cell (DAC) with synchrotron-based single-crystal X-ray diffraction (XRD).

METHODS

The Fe_7C_3 single crystal sample was synthesized at 18 GPa and 1773 K in a multi-anvil press (Prescher et al., 2015). Single-crystal XRD characterizations of the sample at ambient conditions were conducted at beamline 13-BMC, the Advanced Photon Source (APS), Argonne National Lab and at the University of Hawai‘i at Mānoa (UHM) using a Bruker D8 Venture single-crystal diffractometer (λ = 0.5609 Å). The sample was

This is a preprint, the final version is subject to change, of the American Mineralogist (MSA)
Cite as Authors (Year) Title. American Mineralogist, in press.
DOI: https://doi.org/10.2138/am-2018-6527

mounted on a MiTeGen micromesh that was attached to a goniometer head. At beamline 13-BMC, the sample was rotated from -60º to +60º. 120º wide-angle exposure and 1º step exposures were collected. For the ambient characterization of the sample at UHM, a preliminary matrix run was first completed with 1º steps through orthogonal slices of reciprocal space. Indexing of diffraction peaks from the matrix run was used by Bruker APEX 3 software to determine an optimal data collection strategy that ensured 100% completeness to a resolution limit of 0.65 Å. This strategy was then used to collect a full dataset.

A BX90 DAC with a pair of 250 μm-culet diamond anvils was used for the high-pressure XRD experiments (Kantor et al., 2012). A cubic boron nitride seat on the upstream side and a large-opening tungsten carbide seat on the downstream side were used to maximize access to reciprocal space for the single-crystal XRD measurements. A pyrophyllite ring-heater base was fabricated using a milling machine and sintered in a furnace at 1373 K for 20 hours. Three Pt-10wt.%Rh (0.01") wires were wound around the heater base and covered by high-temperature cement. Two K-type thermocouples (Chromega-Alomega 0.005" and Chromega-Alomega 0.010") were mounted near the diamond culet and in touch with the downstream diamond to measure the temperature. The rhenium gasket was preindented to a thickness of ~35 μm and a sample chamber of 150 μm in diameter was drilled by an electrical discharge machine (EDM). A 10 μm thick Fe_7C_3 single-crystal grain and two pressure calibrants, a small ruby sphere (Mao et al., 1986) for the neon gas loading and a piece of gold foil near the sample as the primary pressure scale in experiments (Fei et al., 2007), were loaded in the sample chamber. Neon gas, which was used as a pressure-transmitting medium, was loaded in the sample

This is a preprint, the final version is subject to change, of the American Mineralogist (MSA)
Cite as Authors (Year) Title. American Mineralogist, in press.
DOI: https://doi.org/10.2138/am-2018-6527

chamber using the gas loading machine at GeoSoilEnviroCARS of the APS. The pressure uncertainties were estimated by the pressure difference of gold and neon (Fei et al., 2007).

The high-pressure and high-temperature synchrotron-based single-crystal XRD experiments were conducted at beamline 13-BMC, APS, Argonne National Lab. The typical size of the focused monochromatic X-ray beam (λ = 0.4340 Å) was 16×11 μm^2. A MAR165 charged coupled device (CCD) detector was used to collect the diffraction patterns. The X-ray accessible opening angle of the DAC was ±20º. The rotation axis for the single-crystal diffraction experiment was placed horizontally, perpendicular to the incident X-ray beam. A series of 10º wide-angle exposures and 1º step exposures from -20º and 20º were collected at four different detector positions for each pressure and temperature point. The investigated range of pressure was 1 bar to 79.2 GPa and range of the temperature was 300K to 800K (Fig. S1).

To analyze the synchrotron-based single crystal XRD data, we utilized the ATREX software package for peak fitting and intensity corrections (Dera et al., 2013). The unit cell and orientation matrix were determined by the CELL_NOW software (Bruker AXS Inc.). Lattice parameters were refined by least-squares fitting in the RSV software (Dera et al., 2013). The structure refinement was performed using SHELXL (Sheldrick, 2008). The ambient pressure data collected at UHM were analyzed using the Bruker APEX 3 software package to solve the complexity in the crystal structure. The *P*-*V*-*T* data and *P*-*x* (i.e *a*/*b*/*c* axes) were fitted by the EosFit7-GUI program (Gonzalez-Platas et al., 2016).

RESULTS AND DISCUSSION

This is a preprint, the final version is subject to change, of the American Mineralogist (MSA)
Cite as Authors (Year) Title. American Mineralogist, in press.
DOI: https://doi.org/10.2138/am-2018-6527

The crystal structure of Fe_7C_3 at room pressure and temperature

The indexing of single-crystal XRD patterns of Fe_7C_3 at ambient conditions indicates an orthorhombic lattice with space group *Pbca* (Z = 8), and with unit-cell parameters of a = 11.979(1) Å, b = 4.5191(8) Å and c = 13.767(2) Å. However, the ambient data indicate some structural complexity beyond the simple ideal structure described previously (Prescher et al., 2015), and consistently present in all of the several single crystal specimens that we have examined. This non-ideality involves the presence of twin micro-domains, but seems to also include structural modulation.

The presence of peaks that could not be indexed using a single orientation matrix to the initially indexed domain indicates a likely twinned crystal structure (Fig. S2). The second domain is significantly weaker than the first. A total of 1651 peaks from the dominant domain were utilized to refine the crystal structure (Fig. 1 and CIF in the deposit materials), which is generally consistent with that reported by Prescher *et al.* (2015). In the *Pbca* structure, three distorted CFe_6 triagonal prisms form triads by sharing corners. The triads are stacked parallel to the *b* axis to form a column. Each stack is rotated ~60° relative to its neighbors. Columns are oriented inversely along the *b* axis compared to their neighbor columns. Columns with the same direction are edge sharing and columns with the opposite direction are corner sharing (Fig. 1).

The quality of structural refinement was high (R_{int} = 7.26% and R_1 = 4.97%), however, we noted some artifacts that may be related to the twinning and/or the additional disorder within the structure. Three noticeably large peaks appeared in the difference Fourier map with heights above 2.5 e/Å^3, located about 0.8 Å from carbon atoms, and 1.6 Å from closest Fe atoms. We attempted to reduce the symmetry to

This is a preprint, the final version is subject to change, of the American Mineralogist (MSA)
Cite as Authors (Year) Title. American Mineralogist, in press.
DOI: https://doi.org/10.2138/am-2018-6527

allowed orthorhombic and monoclinic subgroups of *Pbca* but could not find an alternative space group that would better account for this difference electron density. We also noted that the residual electron density reported by Prescher et al. (2015) was also quite high (2.022 e/Å^3), which may indicate similar structural complexity in their samples. Proper refinement of such complexity in the structure may require a description using a 4-dimensional space group and the introduction of an extra basis vector or modulation vector. Additional ambient pressure experiments at varied temperatures are needed to confirm the likelihood of the modulation and whether the modulation is commensurate or incommensurate. Detailed crystallographic studies will be required to determine the exact origin of this difference electron density, but this is out of the scope for the present study which is primarily focused on the thermoelastic behaviors.

Thermal equation of state of Fe_7C_3

The unit cell volumes of Fe_7C_3 along various isotherms from 300K to 800K were determined by synchrotron-based single-crystal XRD measurements up to 79.2 GPa (Fig. S3 and Table S1). No discontinuous crystal-structure change was observed over the entire pressure and temperature range. The room temperature *P-V* data were fitted by the third-order Birch-Murnaghan Equation of State (B-M):

$$P = \frac{3}{2}K_{T_0}\left[\left(\frac{V_{T_0}}{V}\right)^{\frac{7}{3}} - \left(\frac{V_{T_0}}{V}\right)^{\frac{5}{3}}\right] * \left\{1 + \frac{3}{2}(K_{T_0}{}' - 4)\left[\left(\frac{V_{T_0}}{V}\right)^{\frac{2}{3}} - 1\right]\right\} \quad (1)$$

where K_{T_0}, K_{T_0}' and V_{T_0} are the isothermal bulk modulus, its first pressure derivative and the unit cell volume at ambient pressure and given temperature *T*, respectively. The 10 *P-V* data were weighted by the uncertainties in both pressure and volume and fitted by the

This is a preprint, the final version is subject to change, of the American Mineralogist (MSA)
Cite as Authors (Year) Title. American Mineralogist, in press.
DOI: https://doi.org/10.2138/am-2018-6527

third-order B-M EoS with K_0 = 165(4) GPa, K_0' = 5.1(2) and V_0 = 745.3(2) Å^3 (K_0, K_0' and V_0 are for T = 300K). Normalized stress (F_E) as a function of the Eulerian finite strain (f_E) is also plotted as an inset of Fig. 2, where $f_E=[(V/V_0)^{-2/3}-1]/2$ and $F_E= P/[3f_E(1+2f_E)^{5/2}]$ and the EoS can be simplified as $F_E =K_0+3K_0/2(K_0'-4)f_E$, neglecting the high order terms (Angel, 2000). The *f-F* plot can be used to verify which order of the B-M EoS is sufficient to satisfactorily represent the compression behavior of the sample (Angel, 2000). The quasi-linear *f-F* relationship suggests the adequacy of using the third-order B-M EoS and its positive slope indicates $K_0' > 4$ (Fig. 2 inset). Previous studies reported that the slope of the *f-F* plot changed abruptly as a result of the magnetic transitions of hexagonal Fe_7C_3 (Chen et al., 2012; Liu et al., 2016a), but we did not observe this, potentially due to the sparsity of our data at 300K (Fig. 2 inset).

Due to the similarity between the orthorhombic structure with the *Pbca* space group and the hexagonal structure with $P6_3mc$ space group, the compressibility of Fe_7C_3 was compared with the compressibility of both orthorhombic and hexagonal Fe_7C_3 in the previous studies (Table 1 and Fig. 2). Our bulk modulus is consistent with the orthorhombic Fe_7C_3 phase from Prescher et al. (2015), but its pressure derivative, K', is smaller (5.1(2) in this study while 6.1(1) in Prescher et al. (2015)). The discrepancy may be caused by two reasons. First, we used a gold pressure standard whereas Prescher et al. (2015) used ruby as their pressure standard. Second, our experiment involved external heating while the experiments in Prescher et al. (2015) were conducted at room temperature. The larger K' in their studymay indicate less hydrostatic sample chamber with increasing pressure (this is seen in other materials, e.g. Finkelstein et al. (2017). High temperatures could help to relax the deviatoric stress present in the sample chamber.

Comparing with the hexagonal Fe_7C_3 shown in Fig. 2 and Table 1, our density as a function of pressure and compressibility is similar to the values reported by Liu et al. (2016a), who argued that the pressure calibration in his study might be more accurate because the Au pressure standard was placed on the top of the sample.

In our study, Equation (1) was used along various high-temperature isotherms at 300K, 400K, 500K, 600K, 700K, and 800K (Table S1 and Fig. 3). Assuming that dK/dT is constant through the temperature ranges, K_{T0} and K_{T0}' can be described as:

$$K_{T0} = K_0 + \mathrm{d}K/\mathrm{d}T \times (T\text{-}300) \quad (2)$$

$$K_{T0}' = K_0' \quad (3)$$

and the temperature dependence of volume can be expressed by the empirical polynomial equation (Berman, 1988) as:

$$V_{T0} = V_0(1+\alpha_0(T\text{-}300)+\frac{\mathbf{1}}{\mathbf{2}}\alpha_1(T\text{-}300)^2) \quad (4)$$

Taking the first derivative of the Equation (4) gives the thermal expansion coefficient $\alpha_T = \alpha_0\alpha_{+1}(T\text{-}300)$ by approximation. The fit to the P-V-T data (Table S1) using Equations (1-4) results in K_0 = 167(4) GPa, K_0' = 5.0(2) and V_0 = 745.2(2) Å^3, dK/dT = -0.02(1) GPa/K and thermal expansion $\alpha_T = 4.7(9)\times10^{-5}+3(5\times)10^{-8}\times(T\text{-}300)$ K^{-1}. K_0, K_0' and V_0 obtained by the high-temperature Birch-Murnaghan EoS are consistent with the values by only fitting the 300K data within the uncertainties.

Compressibilities and thermal expansions of the *a*, *b* and *c* axes

This is a preprint, the final version is subject to change, of the American Mineralogist (MSA)
Cite as Authors (Year) Title. American Mineralogist, in press.
DOI: https://doi.org/10.2138/am-2018-6527

The compression data of the *a*, *b* and *c* axes at 300 K were fitted by the EosFit7-GUI program (Gonzalez-Platas et al., 2016). The program fits the cube of the lattice parameters to obtain the linear moduli and its pressure derivative, typically denoted as *M* and *M*', respectively (Angel et al., 2014). *M* is the inverse of the linear compressibility β ($\beta_i = x_i^{-1}(\partial x_i/\partial P)_T$) and three times that of the volume-like *K* value (Angel, 2000). The fitting yields M_a = 577(14) GPa, M_a' = 18.6(9), M_b = 438(9) GPa, M_b' = 12.7(4), M_c = 490(32) GPa and M_c' = 16(2). $M_a > M_c > M_b$ indicates that the axial compressibilities of Fe_7C_3 are anisotropic (Fig. 4). Considering the trade-off between *M* and *M*', compressibilities of the *a*, *b* and *c* axes are distinguishable from each other (Fig. 4a inset). Given that M_a'> M_c'> M_b' and considering their magnitudes, the *b* axis would stay the most compressible, ~17.4% smaller than the *c* axis and ~26.5% smaller than the *a* axis in linear modulus at 330-364 GPa (Fig. 4b). The reason that the *a* and *c* axes are less compressible than the *b* axis is that Fe ions are distributed more densely in the same *a*-*c* plane than in the *b* direction, which makes the Fe-Fe bonds shorter and stronger in *a* and *c* directions (Fig. 1). Similar to our results, theoretical calculations by Raza et al. (2015) also indicated that the axial compressibilities of the orthorhombic Fe_7C_3 are discernably anisotropic, and the compressibility of the *b* axis is most obviously different from those of the other axes. The calculated sound velocity (v_p) of Fe_7C_3 in *b* direction is the slowest, while the sound velocities in the *a* and *c* directions are relatively similar at 360 GPa (Raza et al., 2015), which is consistent with our linear incompressibility results.

Thermal expansion of a^3, b^3 and c^3 are also calculated using the Equation (5) (Fig. 5):

This is a preprint, the final version is subject to change, of the American Mineralogist (MSA)
Cite as Authors (Year) Title. American Mineralogist, in press.
DOI: https://doi.org/10.2138/am-2018-6527

$$\alpha = \frac{x_{T(P)}^3 - x_{0(P)}^3}{x_{0(P)}^3 (T - T_0)} \quad (5)$$

We found that the thermal expansions of c^3 (about 8×10^{-5} K^{-1}) from 300K to 600K or 700K were larger than that of a^3 and b^3 by a factor of approximately 4, indicating that there are anisotropic responses of lattice expansion to high temperature along different crystallographic directions (Fig. 6). The anisotropic response was also reflected by an increase in the *c*/*a* ratio upon heating (Fig. 7). The *b*/*a* ratio was nearly unchanged with temperature and the *b*/*c* ratio decreased with temperature (Fig. 7). This means that the significant change of the *c*/*a* ratio with temperature can be mainly attributed to the large expansion of the *c* axis upon heating.

The distinct anisotropic responses could influence the compressibility and sound velocities of Fe_7C_3. For *hcp* iron, the *c*/*a* ratio also increases upon heating and the elastic anisotropy changes, showing that the corresponding longitudinal modulus of *c* axis, C_{33} decreases and becomes smaller than C_{11} (*Steinle-Neumann, 2001*). This suggests that an expanded *c* axis may result in elastic softening along this crystallography direction. One consequence might be a large sound velocity reduction along the *c* axis than the other axes at high temperatures. Although the crystal structure of *hcp* iron is different from that of Fe_7C_3, the change of the *c*/*a* ratios upon heating in Fe_7C_3, resulted from the compressibilities change of the crystallographic axis, may still indicate the change of the elastic anisotropy.

Along the isotherms, the *c*/*a* ratio gradually decreases up to ~40 GPa and then increases abruptly (Fig. 7), probably due to the high-spin to low-spin transition of Fe_7C_3 (Chen et al., 2012; Chen et al., 2014). For higher temperature data, the change occurs at

This is a preprint, the final version is subject to change, of the American Mineralogist (MSA)
Cite as Authors (Year) Title. American Mineralogist, in press.
DOI: https://doi.org/10.2138/am-2018-6527

higher pressures: this is consistent with that high temperature would promote low-spin to high-spin transition in 3d metal compounds (Gütlich et al., 1994) and probably indicates a positive slope for the spin transition (Liu et al., 2016a). The spin transition may have lead to the kink in the *c*/*a* ratio at ~40 GPa at 300K (Fig. 7). After the spin transition, it appears that the *c*/*a* ratio decreases at a similar slope as before the spin transition. The effect of the spin transition on the compressibilities of crystallographic axes is not obvious in this study. We found it was reasonable to use one linear equation of state to describe the compressibilities of crystallographic axes (Fig. 4). Further studies with denser data coverage and to higher pressure are required to further confirm that.

Temperature may significantly influence the elastic properties of Fe_7C_3 at high pressures. When only pressure is taken into account, the *a* and *c* axes of Fe_7C_3 have relatively similar compressibility but the *b* axis is more compressible. According to theoretical calculations, the *b* axis is also the direction along which acoustic waves travel the slowest (Raza et al., 2015). When temperature is considered, the *c* axis expands more significantly than the other axes and thus becomes elastically softer at high temperatures, which suggests that the acoustic wave traveling along the *c* axis may also slow down and influence the elastic anisotropy. At high pressure and temperature conditions like in the inner core, the *a* axis of Fe_7C_3 will stay the most incompressible and thus has the highest sound velocity along *a* axis. Our data implies that temperature is an important factor when considering the anisotropy of Fe_7C_3 at core conditions and caution needs to be exercised for extrapolating to the inner-core conditions.

Seismological data suggest that Earth's inner core exhibits strong elastic anisotropy, an anomalously high Poisson's ratio and low shear-wave velocity (v_S) (Deuss (2014) and the papers cited within). These seismic features are possibly linked to the crystallographic anisotropy of the inner-core crystals. According to the theoretically calculated Fe-C phase diagram at 330 GPa, if an Fe-C liquid has >2wt.% carbon, Fe_7C_3 would crystallize first to form an iron carbide inner core (Fei and Brosh, 2014); the innermost inner core has been further suggested to be Fe_7C_3 based on the melting experiments of the Fe-C system to core pressures (Liu et al., 2016b). With decreasing core temperature and the depletion of carbon in the outer core by the growth of Fe_7C_3 in the inner core, the Fe-C melt will approach the eutectic composition. C-doped Fe and Fe_7C_3 would crystallize from the eutectic composition and form the outer part of the inner core which surrounds the innermost inner core. Our results on the anisotropic compressibility and thermal expansion of the different crystallographic axes of Fe_7C_3 may provide an explanation for the seismic observations of the inner core, particularly the observed inner core anisotropy. The effect of temperature on the elastic properties and anisotropy of Fe alloys such as Fe_7C_3 are crucial for us to construct a seismologically consistent core compositional model and thus inform better understanding of the composition and structure of the inner core. The thermal expansions of iron carbides at high pressures are crucial for modeling the Fe-C phase relations at extreme conditions (Fei and Brosh, 2014), which may inform our understanding of the mineralogy of the inner core and the role of carbon during inner core crystallization.

Acknowledgement

Revision 2

This work was performed at GeoSoilEnviroCARS (The University of Chicago, Sector 13), Advanced Photon Source, Argonne National Laboratory. GeoSoilEnviroCARS is supported by the National Science Foundation-Earth Sciences (EAR-1128799) and Department of Energy-GeoSciences (DE-FG02-94ER14466). This research used resources of the Advanced Photon Source, a U.S. Department of Energy (DOE) Office of Science User Facility operated for the DOE Office of Science by Argonne National Laboratory under Contract No. DE-AC02-06CH11357. Development of the ATREX software, which was used for experimental data analysis was supported by National Science Foundation (NSF) EAR GeoInformatics grant 1440005. Development of the X-ray Atlas instrument was funded by NSF EAR Infrastructure and Facilities grant 1541516. This work was supported by the Bullard award, University of Hawai‘i at Mānoa to XL and NSF grant EAR-1555388 to BC. We are grateful to Danielle Gray for the valuable discussion. We thank the Associate Editor Dr. Sinmyo, the two anonymous reviewers and the Technical Editor for their constructive comments. School of Ocean and Earth Science and Technology (SOEST) contribution ####. Hawaii Institute of Geophysics and Planetology (HIGP) contribution ####.

This is a preprint, the final version is subject to change, of the American Mineralogist (MSA)
Cite as Authors (Year) Title. American Mineralogist, in press.
DOI: https://doi.org/10.2138/am-2018-6527

359 **REFERENCES CITED**

360 Angel, R.J. (2000) Equations of state. Reviews in Mineralogy and Geochemistry, 41(1),
361 35-59.
362 Angel, R.J., Alvaro, M., and Gonzalez-Platas, J. (2014) EosFit7c and a Fortran module
363 (library) for equation of state calculations. Zeitschrift für Kristallographie-
364 Crystalline Materials, 229(5), 405-419.
365 Barinov, V., Tsurin, V., and Surikov, V. (2010) Study of mechanically synthesized
366 carbide Fe_7C_3. The Physics of Metals and Metallography, 110(5), 474-484.
367 Berman, R.G. (1988) Internally-consistent thermodynamic data for minerals in the
368 system Na_2O-K_2O-CaO-MgO-FeO-Fe_2O_3-Al_2O_3-SiO_2-TiO_2-H_2O-CO_2. Journal of
369 Petrology, 29(2), 445-522.
370 Bouchard, J. (1967) Etude structurale des carbures de manganese. Annales de Chimie, 2,
371 353-366.
372 Chen, B., Gao, L., Lavina, B., Dera, P., Alp, E.E., Zhao, J., and Li, J. (2012) Magneto-
373 elastic coupling in compressed Fe_7C_3 supports carbon in Earth's inner core.
374 Geophysical Research Letters, 39(18).
375 Chen, B., Li, Z., Zhang, D., Liu, J., Hu, M.Y., Zhao, J., Bi, W., Alp, E.E., Xiao, Y., and
376 Chow, P. (2014) Hidden carbon in Earth's inner core revealed by shear
377 softening in dense Fe_7C_3. Proceedings of the National Academy of Sciences,
378 111(50), 17755-17758.
379 Dera, P., Zhuravlev, K., Prakapenka, V., Rivers, M.L., Finkelstein, G.J., Grubor-
380 Urosevic, O., Tschauner, O., Clark, S.M., and Downs, R.T. (2013) High pressure

single-crystal micro X-ray diffraction analysis with GSE_ADA/RSV software. High Pressure Research, 33(3), 466-484.

Deuss, A. (2014) Heterogeneity and anisotropy of Earth's inner core. Annual Review of Earth and Planetary Sciences, 42, 103-126.

Fei, Y., and Brosh, E. (2014) Experimental study and thermodynamic calculations of phase relations in the Fe–C system at high pressure. Earth and Planetary Science Letters, 408, 155-162.

Fei, Y., Ricolleau, A., Frank, M., Mibe, K., Shen, G., and Prakapenka, V. (2007) Toward an internally consistent pressure scale. Proceedings of the National Academy of Sciences, 104(22), 9182-9186.

Finkelstein, G.J., Jackson, J.M., Sturhahn, W., Zhang, D., Alp, E.E., and Toellner, T.S. (2017) Single-crystal equations of state of magnesiowüstite at high pressures. American Mineralogist: Journal of Earth and Planetary Materials, 102(8), 1709-1717.

Fischer, R.A., and Campbell, A.J. (2015) The axial ratio of hcp Fe and Fe–Ni–Si alloys to the conditions of Earth's inner core. American Mineralogist, 100(11-12), 2718-2724.

Fruchart, R., Senateur, J., Bouchaud, J., and Michel, A. (1965) A propos de la structure exacte du carbure de fer Fe_7C_3. Bulletin de la Societe Chimique de France (2), 392.

Gonzalez-Platas, J., Alvaro, M., Nestola, F., and Angel, R. (2016) EosFit7-GUI: a new graphical user interface for equation of state calculations, analyses and teaching. Journal of Applied Crystallography, 49(4), 1377-1382.

Gütlich, P., Hauser, A., and Spiering, H. (1994) Thermal and optical switching of iron (II) complexes. Angewandte Chemie International Edition in English, 33(20), 2024-2054.

Herbstein, F., and Snyman, J. (1964) Identification of Eckstrom-Adcock iron carbide as Fe_7C_3. Inorganic Chemistry, 3(6), 894-896.

Hirose, K., Labrosse, S., and Hernlund, J. (2013) Composition and state of the core. Annual Review of Earth and Planetary Sciences, 41, 657-691.

Kantor, I., Prakapenka, V., Kantor, A., Dera, P., Kurnosov, A., Sinogeikin, S., Dubrovinskaia, N., and Dubrovinsky, L. (2012) BX90: A new diamond anvil cell design for X-ray diffraction and optical measurements. Review of Scientific Instruments, 83(12), 125102.

Li, J., and Fei, Y. (2014) Experimental constraints on core composition. 527-557 p. Elsevier Ltd.

Li, Y., Vočadlo, L., Brodholt, J., and Wood, I. (2016) Thermoelasticity of Fe_7C_3 under inner core conditions. Journal of Geophysical Research: Solid Earth, 121(8), 5828-5837.

Litasov, K.D., Rashchenko, S.V., Shmakov, A.N., Palyanov, Y.N., and Sokol, A.G. (2015) Thermal expansion of iron carbides, Fe_7C_3 and Fe_3C, at 297–911K determined by in situ X-ray diffraction. Journal of Alloys and Compounds, 628, 102-106.

Litasov, K.D., and Shatskiy, A. (2016) Composition of the Earth's core: A review. Russian Geology and Geophysics, 57(1), 22-46.

Liu, J., Li, J., and Ikuta, D. (2016a) Elastic softening in Fe_7C_3 with implications for Earth's deep carbon reservoirs. Journal of Geophysical Research: Solid Earth, 121(3), 1514-1524.

Liu, J., Lin, J.F., Prakapenka, V., Prescher, C., and Yoshino, T. (2016b) Phase relations of Fe_3C and Fe_7C_3 up to 185 GPa and 5200 K: Implication for the stability of iron carbide in the Earth's core. Geophysical Research Letters, 43(24), 12,415-12,422.

Lord, O., Walter, M., Dasgupta, R., Walker, D., and Clark, S. (2009) Melting in the Fe–C system to 70 GPa. Earth and Planetary Science Letters, 284(1), 157-167.

Mao, H., Xu, J.-A., and Bell, P. (1986) Calibration of the ruby pressure gauge to 800 kbar under quasi-hydrostatic conditions. Journal of Geophysical Research: Solid Earth, 91(B5), 4673-4676.

Mookherjee, M., Nakajima, Y., Steinle-Neumann, G., Glazyrin, K., Wu, X., Dubrovinsky, L., McCammon, C., and Chumakov, A. (2011) High-pressure behavior of iron carbide (Fe_7C_3) at inner core conditions. Journal of Geophysical Research: Solid Earth, 116, B04201.

Nakajima, Y., Takahashi, E., Sata, N., Nishihara, Y., Hirose, K., Funakoshi, K., and Ohishi, Y. (2011) Thermoelastic property and high-pressure stability of Fe_7C_3: Implication for iron-carbide in the Earth's core. American Mineralogist, 96(7), 1158-1165.

Nakajima, Y., Takahashi, E., Suzuki, T., and Funakoshi, K.-i. (2009) "Carbon in the core" revisited. Physics of the Earth and Planetary Interiors, 174(1), 202-211.

447 Prescher, C., Dubrovinsky, L., Bykova, E., Kupenko, I., Glazyrin, K., Kantor, A.,
448 McCammon, C., Mookherjee, M., Nakajima, Y., and Miyajima, N. (2015) High
449 Poisson's ratio of Earth's inner core explained by carbon alloying. Nature
450 Geoscience, 8(3), 220-223.
451 Raza, Z., Shulumba, N., Caffrey, N.M., Dubrovinsky, L., and Abrikosov, I.A. (2015)
452 First-principles calculations of properties of orthorhombic iron carbide Fe_7C_3 at
453 the Earth's core conditions. Physical Review B, 91(21), 214112.
454 Sheldrick, G.M. (2008) A short history of SHELX. Acta Crystallographica Section A:
455 Foundations of Crystallography, 64(1), 112-122.
456 Steinle-Neumann, G., Stixrude, L., Cohen, R., and Gülseren, O. (2001) Elasticity of iron
457 at the temperature of the Earth's inner core. Nature, 413(6851), 57.
458 Wenk, H., Takeshita, T., Jeanloz, R., and Johnson, G. (1988) Development of texture and
459 elastic anisotropy during deformation of hcp metals. Geophysical Research
460 Letters, 15(1), 76-79.
461 Wood, B.J. (1993) Carbon in the core. Earth and Planetary Science Letters, 117(3), 593-
462 607.
463

This is a preprint, the final version is subject to change, of the American Mineralogist (MSA)
Cite as Authors (Year) Title. American Mineralogist, in press.
DOI: https://doi.org/10.2138/am-2018-6527

464 **FIGURE CAPTIONS**

465

466 Figure 1. The crystal structure of Fe_7C_3 projected along the *b* axis **(left)**, the *a* axis
467 **(upper right)** and the *c* axis **(lower right)** at ambient conditions (space group *Pbca*, *Z* =
468 8). Blue balls represent Fe. One carbon (pink) is located in the center of each CFe_6
469 triagonal prism colored in pink.

470

471 Figure 2. Density of the orthorhombic Fe_7C_3 at 300K in this study compared with other
472 studies. The fitted density using the third-order Birch-Murnaghan EoS is also displayed
473 as the solid line. The solid circles represent the density of orthorhombic Fe_7C_3 in this
474 study. The pressure and density uncertainties are mostly within the symbols. The open
475 symbols are from other studies for comparison (Chen et al., 2012; Liu et al., 2016a;
476 Nakajima et al., 2011; Prescher et al., 2015). Inset is the *F-f* plot of data in this study.

477

478 Figure 3. The *P-V-T* data of Fe_7C_3 fitted by the high-temperature Birch-Murnaghan EoS.
479 The pressure and volume uncertainties are within the symbols. Solid curves are the fitting
480 results.

481

482 Figure 4. The compressibilities of the *a*, *b* and *c* axes of Fe_7C_3 as a function of pressure.
483 **(a)** The variation of a/a_0, b/b_0 and c/c_0 as a function of pressure were fitted by the linear
484 EoS. The uncertainties are mostly within the symbols. Inset: the confidence ellipses for

the *a*, *b* and *c* axes, illustrating the trade-off between M_0 and M'. **(b)** The calculated and extrapolated linear moduli of the *a*, *b* and *c* axes as a function of pressure.

Figure 5. The high-temperature **(a)** a/a_0, **(b)** b/b_0 and **(c)** c/c_0 of Fe_7C_3 versus pressure. The room-temperature data were fitted by the linear EoS.

Figure 6. Thermal expansion of a^3, b^3 and c^3 axes of Fe_7C_3 at 600K and 700K. Open symbols represent the calculated thermal expansion for different axes. Dashed lines are guide lines showing the thermal expansion of c^3 is approximately 4 times larger than a^3 and b^3.

Figure 7. The **(a)** c/a ratio, **(b)** b/c ratio and **(c)** b/a ratio of Fe_7C_3 up to 800K as a function of pressure.

This is a preprint, the final version is subject to change, of the American Mineralogist (MSA)
Cite as Authors (Year) Title. American Mineralogist, in press.
DOI: https://doi.org/10.2138/am-2018-6527

500 Table 1 The thermoelastic properties of Fe_7C_3 compared with previous studies.

	P range (GPa)	*T range* (K)	K_0 (GPa)	K_0'	Normalized V_0 (Å^3)[a]	Thermoelastic properties	Method	Reference
					Orthorhomic (*Pbca*)			
	0-79.2	300	165(4)	5.1(2)	93.2(3)	___	SCXRD+DAC	This study
						dK/dT = -0.02(1) GPa/K		
	0-79.2	300-800	167(4)	5.0(2)	93.2(3)	a_0 = 4.7(9)*10^{-5} K^{-1}	SCXRD+DAC	This study
						a_1 = 3(5)*10^{-8} K^{-2} [b] ___		
	4-158	300	168(4)	6.1(1)	93.1 (1) Hexagonal		SCXRD+DAC	Prescher et al. (2015)
					(*P*6$_3$*mc*)			
ferromagnetic	0-18	300	201 (2)	4 (fixed)	93.2(1)	___	PXRD+DAC+multianvil press	Nakajima et al. (2011)
paramagnetic	18-71.5	300-1973[†]	253 (7)	3.6(2)	92.1 (3)	γ(5)2.57= $_0$ θ= 920 (140) K q = 2.2(5)	PXRD+DAC+multianvil press	Nakajima et al. (2011)
ferromagnetic			231	4.4	91			
nonmagnetic			291	4.5	88			
paramagnetic	7-53	300	201 (12)	8.0 (1.4)	92.4 (2)	___	SCXRD+DAC	Chen et al. (2012)
nonmagnetic	53-167	300	307 (6)	3.2 (1)	91.5 (4)	___	SCXRD+DAC	Chen et al. (2012)
	0	297-911	___	___		a_0 = 3.1(6)*10^{-5} K^{-1} a_1 = 1.2(6)*10^{-8} K^{-2}[c]	PXRD	Litasov et al. (2015)
ferromagnetic	0-7	300	186(5)	6.9(2.2)	93.1 (1)	___	PXRD+DAC	Liu et al. (2016a)
noncollinear	7-20	300	166(13)	4.9 (1.1)	93.5(4)	___	PXRD +DAC	Liu et al. (2016a)
paramagnetic	20-66	300	196(9)	4.9 (2)	92.3 (5)	___	PXRD +DAC	Liu et al. (2016a)

501 Notes： SCXRD and PXRD are acronyms of single-crystal XRD and powder XRD,

502 respectively.

503 [a] Normalized V_0 represents volume per Fe_7C_3 formula.

504 [b] The coefficient of thermal expansion was calculated as $\alpha = \alpha_0 \alpha + {}_1 \times (T\text{-}300)$.

This is a preprint, the final version is subject to change, of the American Mineralogist (MSA)
Cite as Authors (Year) Title. American Mineralogist, in press.
DOI: https://doi.org/10.2138/am-2018-6527

505 [c]The coefficient of thermal expansion was calculated as $\alpha = \alpha_0 + \alpha_1 \times T$.

This is a preprint, the final version is subject to change, of the American Mineralogist (MSA)
Cite as Authors (Year) Title. American Mineralogist, in press.
DOI: https://doi.org/10.2138/am-2018-6527

Revision 2

506

Figure 1

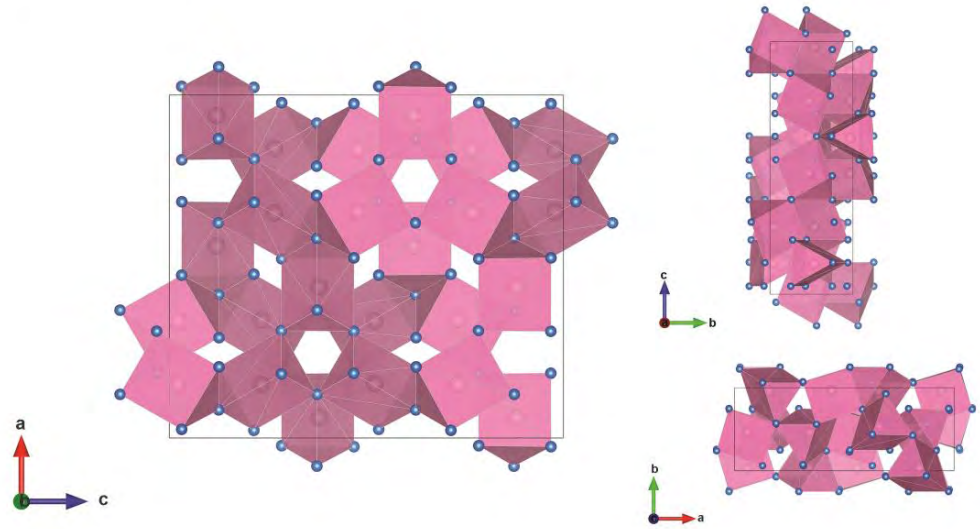

507

508 Figure 1

509

510

511

512

513

Revision 2

Figure 2

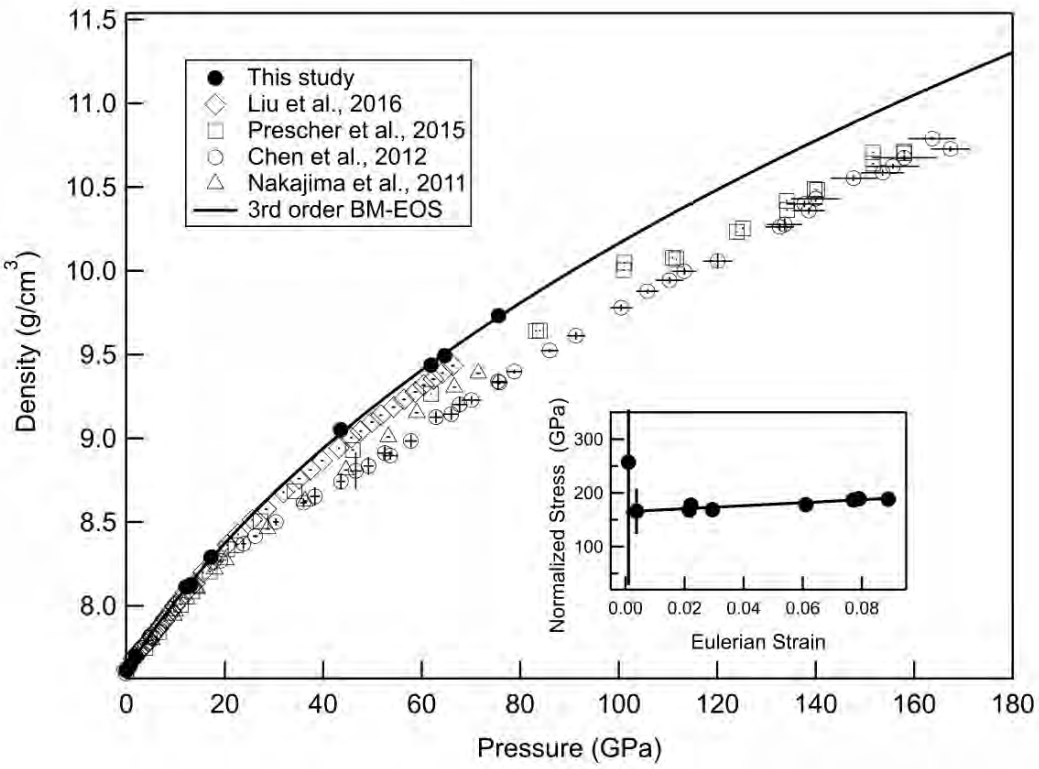

514

515 Figure 2

516

517

This is a preprint, the final version is subject to change, of the American Mineralogist (MSA)
Cite as Authors (Year) Title. American Mineralogist, in press.
DOI: https://doi.org/10.2138/am-2018-6527

Revision 2

Figure 3

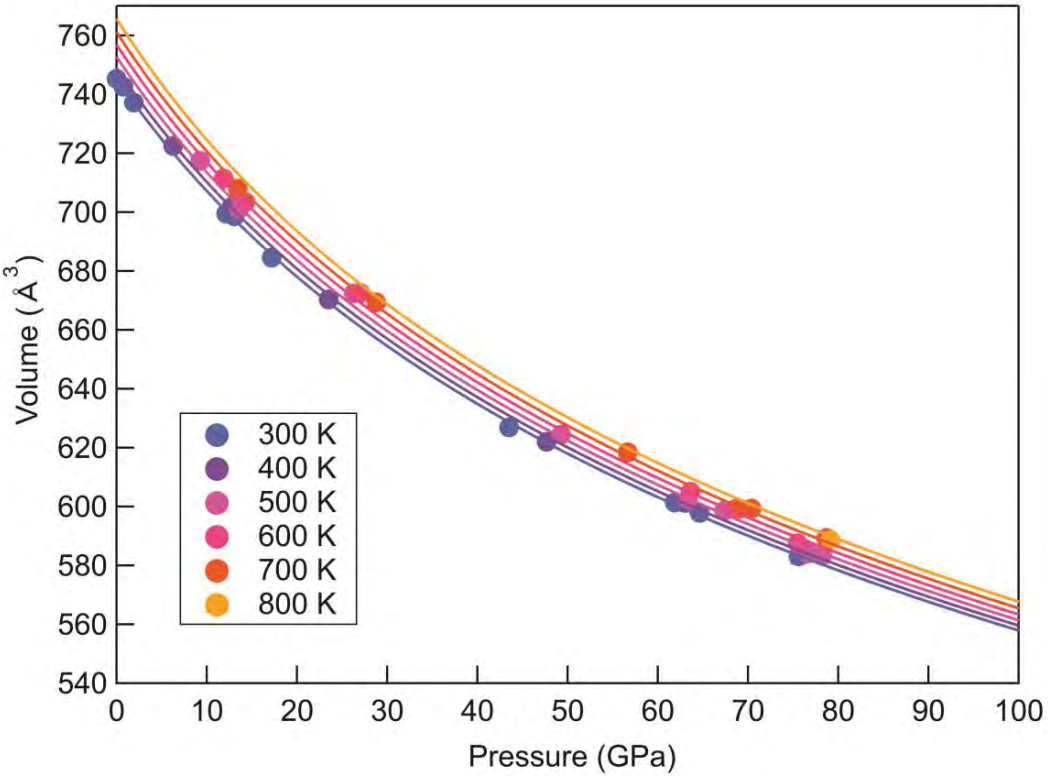

Figure 3

This is a preprint, the final version is subject to change, of the American Mineralogist (MSA)
Cite as Authors (Year) Title. American Mineralogist, in press.
DOI: https://doi.org/10.2138/am-2018-6527

Revision 2

Figure 4

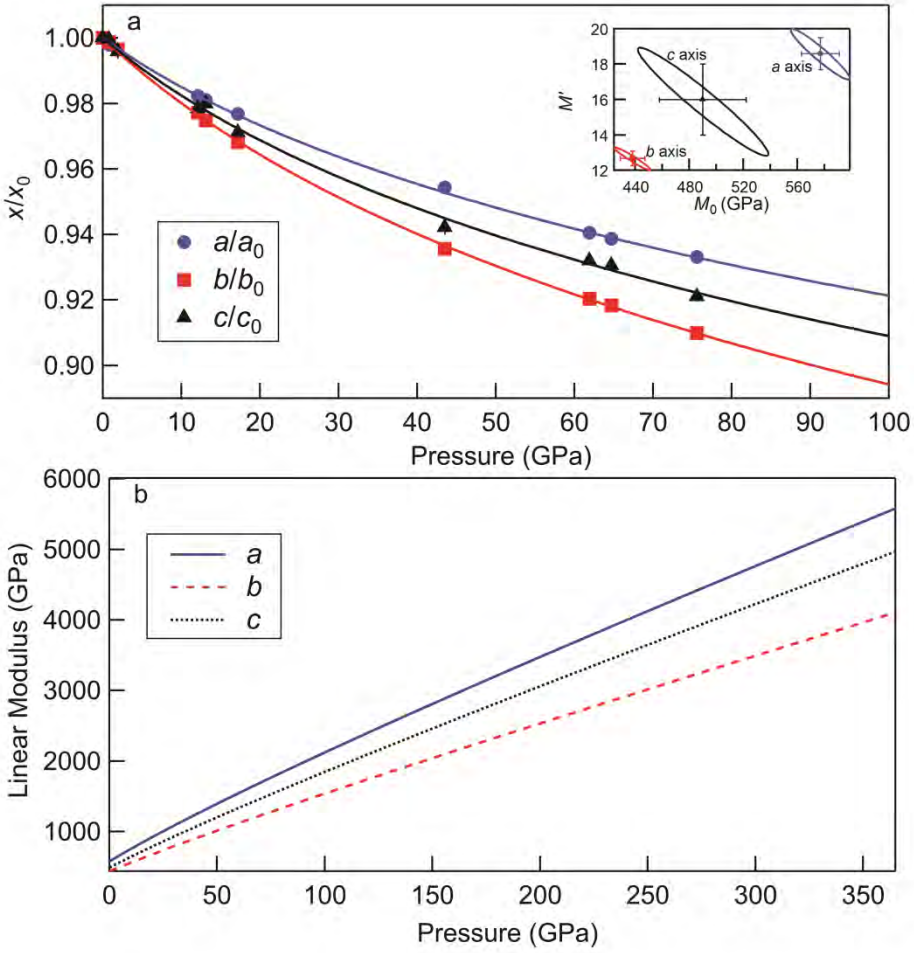

521

522 Figure 4

This is a preprint, the final version is subject to change, of the American Mineralogist (MSA)
Cite as Authors (Year) Title. American Mineralogist, in press.
DOI: https://doi.org/10.2138/am-2018-6527

Revision 2

Figure 5

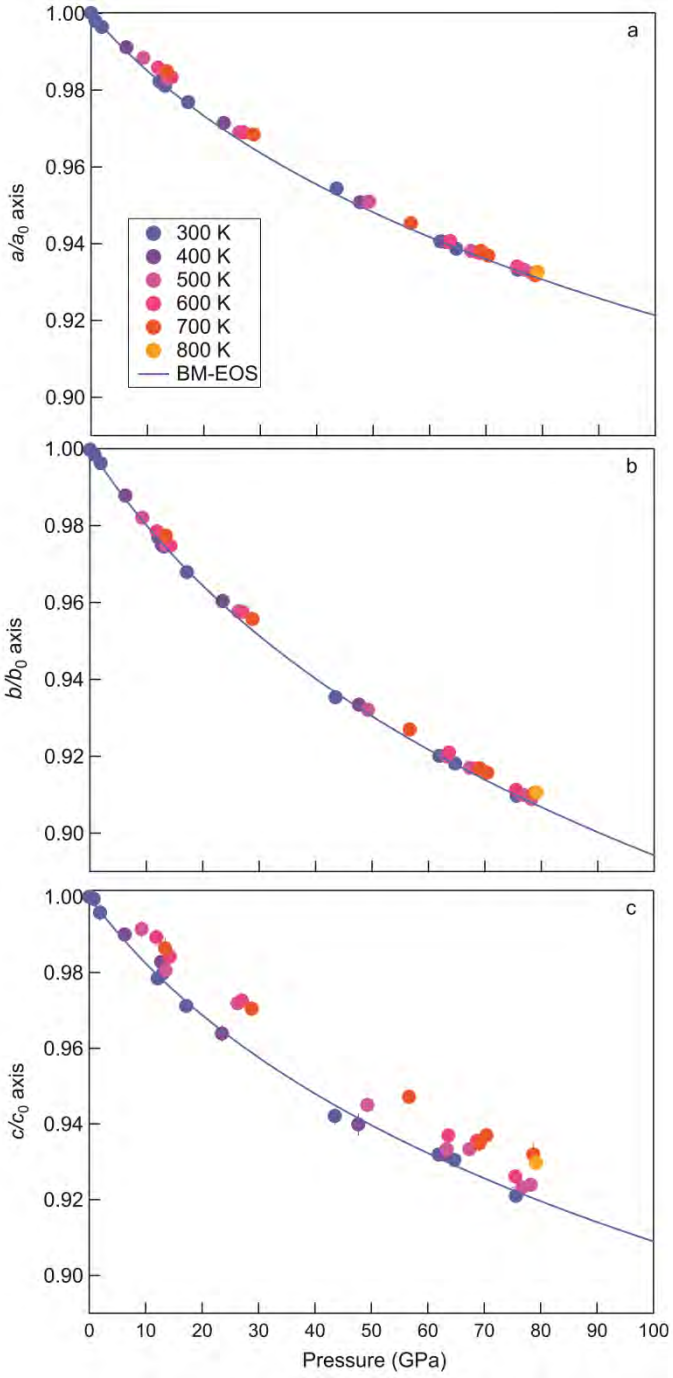

523

524 Figure 5

This is a preprint, the final version is subject to change, of the American Mineralogist (MSA)
Cite as Authors (Year) Title. American Mineralogist, in press.
DOI: https://doi.org/10.2138/am-2018-6527

Revision 2

Figure 6

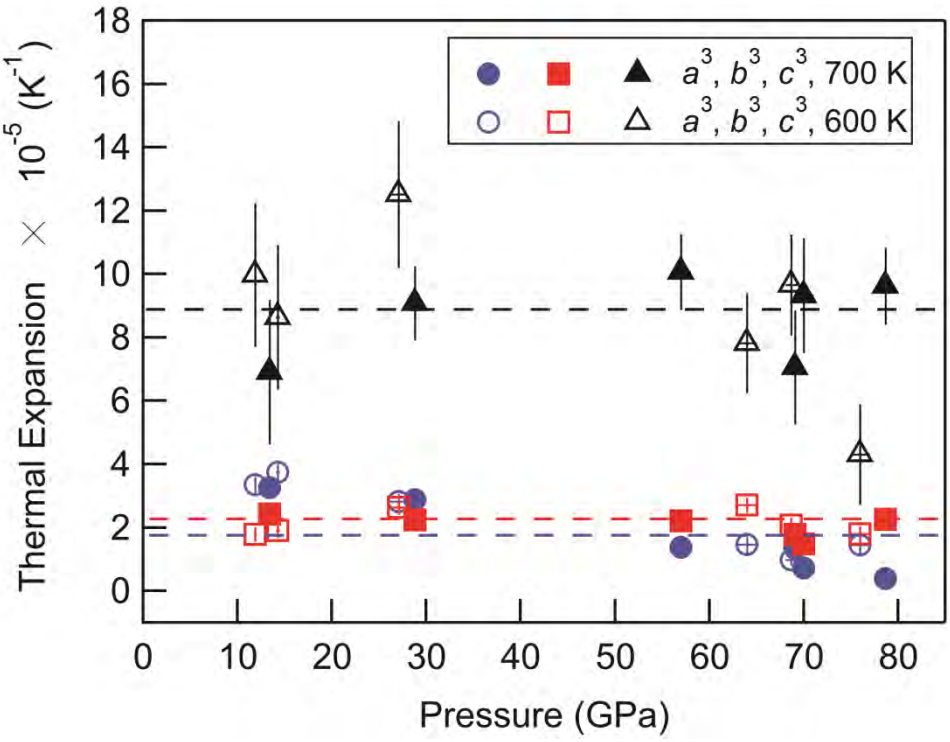

525

526 Figure 6

This is a preprint, the final version is subject to change, of the American Mineralogist (MSA)
Cite as Authors (Year) Title. American Mineralogist, in press.
DOI: https://doi.org/10.2138/am-2018-6527

Revision 2

Figure 7

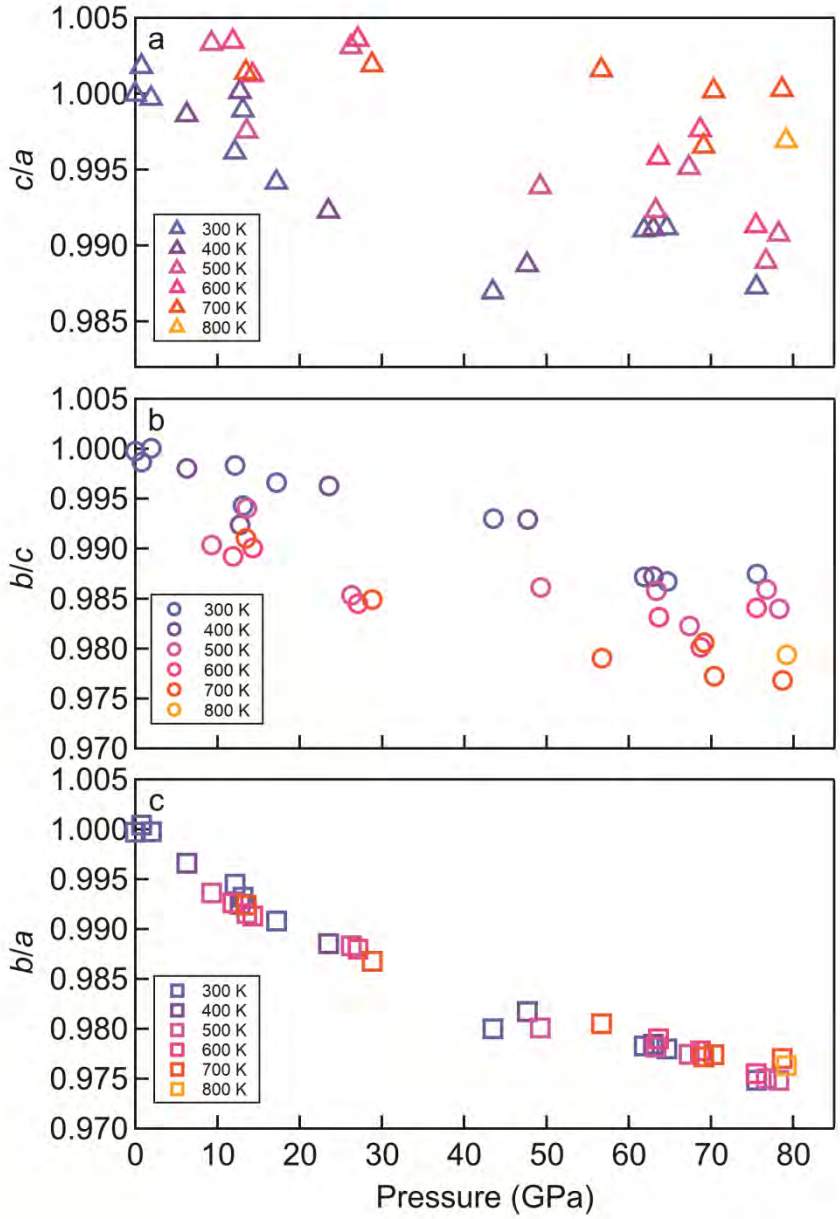

527

528 Figure 7

529

530